Journal of Micromechanics and Microengineering

PAPER • **OPEN ACCESS**

Channel integrated optoelectronic tweezer chip for microfluidic particle manipulation

To cite this article: Christian Witte *et al* 2020 *J. Micromech. Microeng.* **30** 045004

OPEN ACCESS
IOP Publishing
Journal of Micromechanics and Microengineering
J. Micromech. Microeng. **30** (2020) 045004 (12pp)
https://doi.org/10.1088/1361-6439/ab6c72

Channel integrated optoelectronic tweezer chip for microfluidic particle manipulation

Christian Witte, Julien Reboud, Jonathan M Cooper and Steven L Neale

James Watt School of Engineering, University of Glasgow, Glasgow, United Kingdom

E-mail: Steven.Neale@glasgow.ac.uk

Received 1 October 2019, revised 13 December 2019
Accepted for publication 16 January 2020
Published 20 February 2020

Abstract

Light patterned electrical fields have been widely used for the manipulation of microparticles, from cells to microscopic electronic components. In this work, we explore a novel electromechanical phenomenon for particle focusing and sorting where the electrical field patterns are shaped by a combination of the light patterned photoconductor and the channel geometry. This effect results from the combination of particle polarisation described by the Clausius–Mossotti relation and the engineering of large electric gradients produced by choosing the channels height to suit the size of the particles being manipulated. The matched geometry increases the distortion of the field created by a combination of the illuminated photoconductor and the particles themselves and hence the non-uniformity of the field they experience. We demonstrate a new channel integration strategy which allows the creation of precisely defined channel structures in the OET device. By defining channels in photoresist sandwiched between upper and lower ITO coated glass substrates we produce robust channels of well controlled height tailored to the particle. Uniquely, the top substrate is attached before photolithographically defining the channels. We demonstrate versatile control using this effect with dynamically reconfigurable light patterns allowing the retention against flow, focusing and sorting of micro particles within the channels. Contrary to traditional designs, this channel integrated device allows patterned micro channels to be used in conjunction with conductive top and bottom electrodes producing optimal conditions for the dielectrophoretic manipulation as demonstrated by the rapid flow (up to 5 mm s^{-1}) in which the particles can be focused.

Keywords: optoelectronic tweezing, dielectrophoresis, microfluidics, micromanipulation

Supplementary material for this article is available online

(Some figures may appear in colour only in the online journal)

Nomenclature

aSi	Amorphous silicon
CM	Clausius–Mossoti factor
DEP	Dielectrophoresis
ITO	Indium tin oxide
OET	Optoelectronic tweezer
F_{DEP}	Dielectrophoresis force, N
F_D	Stoke's drag force, N
a	Particle radius, m
$\varepsilon_r\varepsilon_0$	Permittivity of the medium
E	Electric field strength, V m^{-1}
$\mathrm{Re}\,[K(\omega)]$	Clausius–Mossoti factor
ε_p	Permittivity of particle, F m^{-1}
ε_m	Permittivity of medium, F m^{-1}
σ	Material conductivity, S m^{-1}

ω	Angular frequency, rad s^{-1}
η	Dynamic viscosity, Pa s
v	Particle velocity, m s^{-1}

1. Introduction

Light patterned electrical fields are a rapidly developing non-contact alternative for the manipulation of microscopic objects to traditional approaches such as probes, micro needles or pipettes. Applications include the patterning, sorting and sequestration of cells into predestined pens in research and industrial settings [1, 2]. The use of moving light patterns in optoelectronic tweezer (OET) devices [3, 4] or virtual sieves [5] have been used for the manipulation and separation of different cell types, DNA [6] the purification of circulating tumour cells [7] as well as the electroporation [8], transfection [9] and lysis of cells [10–12]. OET has also proven to be useful for cell analysis such as determining a cell's physical properties [13] or discrimination between healthy and non-viable cells [5] and development stages of complex systems such as mouse embryos [14], identifying viable sperm cells [15] and healthy oocytes for fertilisation experiments [16]. As well as these varied life science applications OET has also been developed for use in a second area, namely the assembly of sub-millimetre electronic and electrical devices. From original work assembling nanoparticles [17] and nanowires (separating metal and semiconductor nanowires, lateral OET with PL nanowires) this has recently been extended to the manipulation of standard electrical components with dimensions in the hundreds of microns. Surface Mount Technology components such as capacitors [18], integrated circuit (IC) chips [19] and optoelectronic components from micro disk lasers [20] to standard InP laser die [21] have all been assembled with OET. The motivation for manipulating these components is to develop a printer like assembly system that could, instead of printing with ink, print electrical components onto a circuit [19]. Recently micro robots controlled by OET have been demonstrated that can manipulate mammalian cells and other micro objects [22]. For this to be achieved, or for the potential biological applications to be realised, there is a need to integrate OET into a microfluidic channel. This is hindered by the need for the top of the channel to be conductive to give the top electrode of the device and for the bottom surface of the channel to be photoconductive to give the pattern-able electrode. This cannot be achieved with standard PDMS soft lithographic fabrication techniques and has limited many studies to batch processing without the benefit of a flow channel.

The inherent need for microfluidics integrated with the OET device has prompted several groups to develop varied approaches including patterning SU-8 then epoxy gluing the top substrate to the channel walls [23–26], using PDMS modified with gold/titanium mesh or carbon nanotubes as the top electrode and channel structure [27] and defining the channel in a hydrogel placed on a spin coated organic photoconductive layer [24]. These approaches suffer from incomplete bonding [23], weak forces [27] or low durability and incompatibility with solvents [24].

In this work, we demonstrate the integration of precisely controlled channels into a robust microfluidic chip that allowed us to tune the electric properties of the OET chip. The process we developed uses negative photoresist (SU8 3000 series) to create microfluidic channels. As shown in previous studies, SU8 has good adhesion to glass, mechanical and chemical stability making it an excellent material for many microelectromechanical system applications. Moreover, lithography-defined SU8 structures and layers have shown to be biocompatible making it a suitable material for mammalian cell handling applications.

2. Materials and methods

2.1. OET principle

The conventional optoelectronic tweezing device structure (figure 1) consists of transparent top and bottom ITO coated glass electrodes while one of the electrodes (bottom) is covered with a photoconductor such as amorphous silicon (aSi). A bias across the plates and selective illumination of the aSi creates a patterned electrical field in a liquid placed between the plates whose gradients place dielectrophoresis forces onto any polarizable particle present as [28];

$$F_{\mathrm{DEP}} = 2\pi a^3 \varepsilon_r \varepsilon_0 \,\mathrm{Re}\left[K(\omega)\right] \nabla E^2. \tag{1}$$

Here, a is the radius of the particle. $\varepsilon_r\varepsilon_0$ is the absolute permittivity of the medium. ∇E^2 is the gradient of the electric field squared. $\mathrm{Re}\left[K(\omega)\right]$ is the real part of the Clausius–Mossoti factor (CM) which is defined through frequency dependent properties of the materials (particle/medium). The CM factor determines whether the DEP force is directed towards regions of low (negative DEP) or strong (positive DEP) electric fields and is given by [28]:

$$K(\omega) = \left(\frac{\varepsilon_p^* - \varepsilon_m^*}{\varepsilon_p^* + 2\varepsilon_m^*}\right), \quad \varepsilon_{p/m} = \varepsilon_r\varepsilon_0 - j\left(\frac{\sigma}{\omega}\right). \tag{2}$$

Here, ε_p^* and ε_m^* are the complex permittivity of the particle and the medium, σ the conductivity of the materials and ω the angular frequency of the applied AC signal.

To estimate the DEP force acting on the particles retention experiments were carried out. Particles were trapped against the laminar flow (parabolic flow profile at low Reynold's number of 10^{-2}) by balancing the negative DEP force against the drag force F_D:

$$F_D = 6\eta\pi a v \tag{3}$$

where η is the viscosity of the fluid medium (10^{-4} Pa s), a the particle radius and v the velocity of the particle (10^{-4} m s^{-1}). We scaled the force ($3\times$) according to Faxen's corrections assuming particles being close to the surface [29].

2.2. Device fabrication

High resolution polymer-emulsion film masks (JD Photo, UK) were used to fabricate microchannels by photolithographically patterning SU8 3050 and 3025. ITO coated standard glass slides (H: 1 mm × D: 25 mm × L: 75 mm) and cover

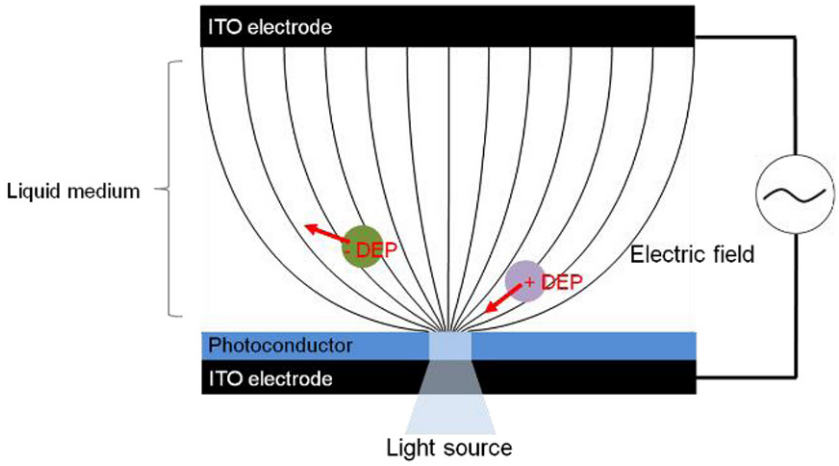

Figure 1. Conventional OET device structure, in which the illumination creates a virtual electrode, generating an electric field gradient. Particles are either attracted or repelled by DEP, depending on the CM factor.

slips (H: 0.16 mm × D: 22 mm × L: 40 mm) were purchased from Diamond Coatings Ltd. (UK). The thickness of the ITO layer was approximately 300 nm. The sheet resistance for the glass slides and glass cover slips were 15 ohms per square and 30 ohms per square. Slides coated with ITO were thoroughly ultrasonically cleaned in acetone, methanol and pure deionised water before coating with 1 μm amorphous silicon layer by plasma-enhanced chemical vapour deposition using pure silane gas (10 W, 300 mTorr, 250 °C, 15 sccm).

The OET chip was constructed from an ITO and aSi coated glass slide and an ITO coated cover slip. First, the ITO cover slip had inlet and outlet holes drilled according to the microchannel mask design. A Dremel drill (MultiPro, Robert Bosch GmbH, Germany) mounted to a work station was used in conjunction with Tungsten drill bits of 0.5 mm diameter (Diama, UK). The substrates were then cleaned in acetone, methanol and deionised water. This was followed by a dehydration bake at 90 °C for 30 min. The OET chip was assembled by sandwiching SU8 between the modified cover slip and glass slides. SU8 has good tensile (73 MPa) and dielectric strength (115 V μm^{-1}). SU8 3050 and SU8 3025 have different viscosities. SU8 3050 has a viscosity of 12000 cSt, while SU8 3025 has a viscosity of 4400 cSt. With that, each SU8 resist yields a different thickness on top of the photoconductor when adjusting the spin coating speed. SU8 3050 was spin coated at 1000 rpm and 4000 rpm for 30 s with an initial coating step at 500 rpm for 10 s. SU8 3025 was spin coated at 500 rpm for 10s followed by 4500 rpm for 30 s. After spin coating the substrate was placed on the hotplate at 95 °C. The cover slip containing predrilled holes for inlets and outlets was bonded immediately onto the freshly prepared SU8 film by carefully placing it on top of the bottom substrate with a small overhang of several millimetre to provide wire connection points. This was followed by a soft bake at 95 °C for 25 minutes, 45 min and 20 min for SU8 3050 coated at 4000 rpm, 1500 rpm and SU8 3025 coated at 4500 rpm, respectively. Following the soft bake, the SU8 was exposed (i-line, 365 nm, 200 mJ cm^{-3}, Mask aligner MA 6, SÜSS MicroTec AG, Germany) through the mask aligned to the predrilled holes in the cover slip for 60 s and 90 s, for SU8 3050 (4000 rpm), SU8 3025 (4500 rpm) and SU8 3050 coated at 1500 rpm, respectively. The post exposure bakes for SU8 3050 (4000 rpm), SU8 3025 (4500 rpm) and SU8 3050 (1500 rpm) coated substrates were set to 5 min and 10 min at 95 °C with an initial bake at 65 °C for 2 min. The developing of the unexposed SU8 was performed through drilled inlet and outlet holes using Microposit EC solvent (Shipley, USA). The whole chip was placed in a beaker containing the developer. The developing process was monitored by observing the phase change (from solid to liquid) of the unexposed SU8 in the microchannel. A clear interface between the solid and the liquid phase was visible during this process. Once the interface vanished, the unexposed SU8 was fully dissolved. To remove any residues left in the channel structures, the chip was placed in an ultrasonic bath with acetone for 5 min to 10 min. The chip was rinsed with acetone, followed by blow drying until the acetone inside the chip was fully removed. The inlet and outlets were connected to PTFE tubing (#30, Cole and Parmer, UK) using shortened 10 μl pipette tips glued to the substrate.

The wire connection points were cleaned by stripping the unexposed SU8 using acetone. On the bottom aSi substrate, the aSi layer was scratched off using a sharp blade and opening a connection point to the ITO layer underneath. Wires were connected with conducting silver paint prior to strong fixation by applying epoxy glue (BondLoc, UK).

Dektat profilometer, SEM and standard brightfield microscope were used to characterise lateral and vertical dimensions of the fabricated OET chips.

2.3. Experimental setup

A TG5011 (TTi, UK) signal generator was used to apply AC signals to the OET chip. A microscope (BX51, Olympus, Japan) equipped with a dual port (U-DP, Olympus, Japan) attachment was used for observation of the micromanipulation and for camera recordings as well as image projection onto the photoconductor (setup shown in figure S1 (stacks.iop.org/JMM/30/045004/mmedia)). The dual port allowed for simultaneous operation of camera and data projector (Dell 1510X). An Orca Flash4.0 CMOS-camera (Hamamatsu,

Japan) was used for recordings. The projector was connected to a PC and images for light induced electric fields were created using the drawing toolset in Microsoft PowerPoint. The microscope was equipped with a 4 × (NA: 0.1), 10 × (NA: 0.4), 20 × (NA: 0.4) and 40 × (NA: 0.65) objectives. An increase in the numerical aperture increased the sharpness of the light pattern as well as the light intensity. Measurements of the optical power using an optical power meter (Wilcom FM1318, USA) resulted in a power range shown in table S1. These values were converted into optical intensities and then corresponding aSi conductivities (figure S2).

Spherical polystyrene microparticle (Bangs Laboratories) of different sizes (3 μm, 6 μm, 10 μm) were suspended in deionised water containing 0.1% tween 20. The conductivity was adjusted by adding potassium chloride to the deionised water and tween 20 suspension prior to the addition of the particles. The suspension was injected into the chip using a syringe pump (NE-1000, New Era Pump Systems, USA). Recordings of particle retentions experiments were analysed using ImageJ (v1.47). The velocities of moving particles under various conditions were extracted to quantify retention and focussing capabilities and DEP forces.

2.4. Device simulation

In order to understand the device characteristics of a micro scaled OET device a range of simulations were undertaken using the finite-element modelling software COMSOL Mutliphysics (v3.5, AC/DC module, in-plane electric currents). A simple 2D cross-section model which depicts the liquid layer and the photoconductor layer in the OET device and their actual thicknesses was used to introduce field distributions, magnitudes and components in the microdevice before the influence of parameters such as the conductivity of the liquid medium and the photoconductor, vertical channel dimensions, electrode pattern sizes as well as potential drops across the layers were specifically explored by experiments. Figure S3 outlines the boundary conditions as well as subdomains used for the model. It describes a typical configuration for a conventional OET device. The model parameters for the different materials are shown in table S2. The photoconductive effect was modelled as a change in the electrical conductivity of the aSi layer. The microscope in this work was equipped with a set of different objectives leading to different optical powers and hence different light intensities (figure S2). The influence of light intensity on the conductivity of the aSi layer was considered by defining values for the dark- and light-state for each objective. To simplify the model the ITO layer was removed as the potential change across it is negligible. The sides of the cross-section were assumed to be electric insulators owing to the fact that a polymer (SU8) was used as microchannel wall in this work. The upper side of the geometry was given an electric potential, while the lower side of the photoconductor was set as ground ($V = 0$). The enclosed sides (interfaces to layers) were subjected to the continuity boundary condition. The layers of the OET device were defined as subdomains and specified by defining geometrical.

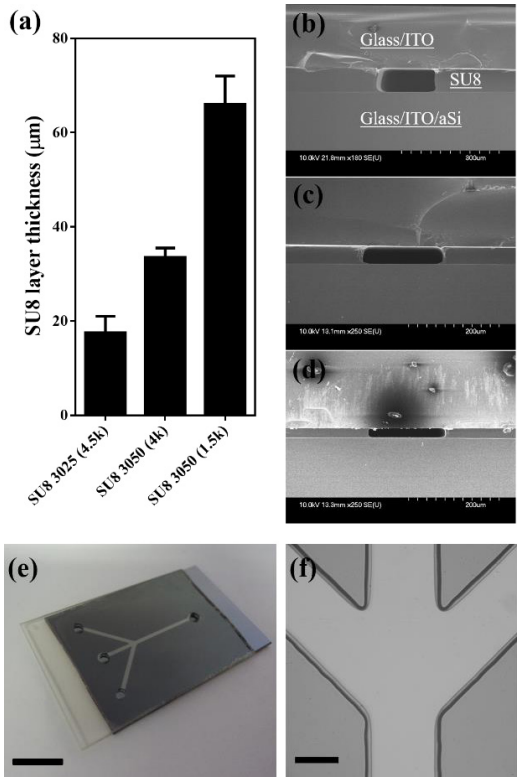

Figure 2. (a) SU8 layer thicknesses of OET devices for different SU8 resists (3050, 3025) and spin coating speeds. (b)–(d) SEM images of OET devices with SU8 layer thicknesses of 70 μm, 35 μm and 15 μm. (e) Bonded OET device with drilled inlet and outlets and overlapping electrode sites for wire connections (Scale bar: 1 cm). (f) Microscope image of a microchannel in the OET device (Scale bar: 100 μm).

GNU Octave (v3.6.4) was used to model the dielectrophoretic response of different sized particles under varying conditions.

3. Results and discussion

3.1. OET Device fabrication

Integration of the conventional OET structure was achieved by sandwiching the photoresist SU8 between the OET electrodes before photopatterning. The resist acted as bonding agent and the microchannel defining layer with adjustability in terms of layer thickness and channel layout. The former was controlled by tuning the spin-coating speed while the latter was defined by the mask layout. Channel thicknesses of 15 μm to 70 μm were achieved using SU8 3000 series (SU8 3025, SU8 3050) and spin coating speeds of 4500 rpm to 1500 rpm (figure 2(a)). Figures 2(b)–(f) shows SEM images of cross-sections of fabricated OET devices with integrated microchannels and an example OET device. It has to be noted that the standard SU8 protocol had to be altered to cater for the unconventional fabrication process. This included pre-bake and exposures times to ensure strong bonding of the OET electrodes and well-defined channel layouts. For instances pre-bake times and exposure times have been increased to reduce solvent content of the SU8 layer after ITO cover slip bonding and compensate UV light absorption losses in the ITO layer. The resulting

microchannels were characterised by a round channel-wall profile, likely due to the sandwich structure, adhesion properties of the resist and the action of developing along the channel rather than from the top. Lateral channel dimensions were not true to the original mask layout but slightly increased as result of mask to resist distance of 160 μm–190 μm (the thickness of the top ITO coated cover slip). Overall, microchannels were residue free once developed (figure 2(f)), the bonding area of the OET electrodes with the SU8 was 100% and the OET chips were durable (leakage-free), and reusable during experiments when conducting appropriate wash and rinsing steps using aqueous and organic solvents.

3.2. OET Device characterisation

3.2.1. AC amplitude dependency. The dielectrophoretic performance of the OET chips were characterised by particle retention experiments where the particles experienced negative DEP imposed by a virtual electrode projected along the width of the microchannel (figure 3(a)). The DEP force was calculated from bead velocity measurements once the drag force was balanced against the negative DEP force under continuous fluid flow. DEP force scaling was investigated by increasing voltage amplitude and flow rates while keeping the frequency at 50 kHz, using an optical power of 2 W cm^{-2}, a virtual electrode width of 45 μm and medium conductivity of 5 mS m^{-1}. The DEP force scales with the square of the gradient of the electric field (equation (1)). Hence, the field should be proportional to the square of the applied voltage. However, our results demonstrated a rather linear relationship in the developed OET device (figure 3(b)). A voltage range from 2.5 V to 20 V enabled retention of particle with velocities of 15 μm s^{-1} to 522 μm s^{-1}, corresponding to DEP forces of 4 pN to 150 pN. The electric field gradient under these conditions is shown in the simulations in figure 3(c) for a voltage amplitude of 20 V. The highest field magnitudes at distances of 2.5 μm to 5 μm to the aSi surface varied between $2.2 \cdot 10^{17}$ V^2 m^{-3} to $8.0 \cdot 10^{15}$ V^2 m^{-3} and can be found at the edges of the virtual electrode. The direction of the DEP force for insulating particles is indicated by black arrows in the surface plot. A negative DEP force with lateral and vertical components was acting on the polystyrene beads resulting in repulsion from high field regions. The exact reason for the linear relationship between DEP force and applied voltage was unclear and requires more investigations. However, one may attribute this effect to the particles being unable to experience the full negative DEP force at higher speeds because of an upward motion. The vertical and the lateral field components scale both with the applied voltage while having a similar magnitude. Under the influence of the negative DEP force a lifting of particles attributed to the vertical field component may reduce the retention effect induced by the lateral field component. This would result in a movement of particles towards lower field regions near the top electrode which then allowed particles to pass the virtual electrode where the drag force overcomes the DEP force. The described behaviour was supported by simulations of the components of ∇E^2. In figure 3(e), ∇E_y^2 and ∇E_x^2 were determined for different voltages and distances from the virtual electrode edge in the photoconductor layer. At distances relative close to the surface, where the DEP force had its maximum, ∇E_y^2 was dominating over ∇E_x^2. This promoted upward motion of particles over the potential barrier and decreased the retention effect. Recently, this phenomenon has also been described by Zhang *et al* who used a conventional OET setup without continuous fluid flow but dynamic light pattern [30].

3.2.2. Influence of medium conductivity. The medium conductivity is a crucial parameter when using conventional OET devices. The developed OET chip can be understood as a simple lumped equivalent circuit containing impedance elements which represent the photoconductor and the liquid medium (figure 4(a)). The applied voltage drops across the photoconductor in the absence of light. The impedance of the photoconductor is higher compared to the liquid medium. When the photoconductor is illuminated the voltage drops across the liquid creating an electric field. The latter case requires the impedance of the liquid and hence the conductivity to be sufficiently low. The voltage drop across the photoconductor was modelled for different medium conductivities (figure 4(b)). The model depicts a voltage drop across the centre of the illuminated area on the photoconductor layer for medium conductivities of 5 mS m^{-1} to 100 mS m^{-1} using an AC signal of 20 V at 50 kHz and a light intensity of 2 W cm^{-2}. At low conductivities (5 mS m^{-1}) the voltage dropped mainly across the liquid layer generating a strong non-uniform electric field. At high medium conductivities (100 mS m^{-1}) the voltage dropped mainly over the photoconductor producing a low electric field magnitude in the liquid layer.

The performance of the OET device was tested at varying liquid conductivities using retention experiments as described above. It has to be noted that an appropriate particle size (10^{-5} m) should be used for this experiment. From equation (2), it is known that the CM factor is dependent on the frequency and the complex permittivity of particle and medium. When the liquid conductivity increases the CM factor decreases. From equation (1) it is clear, the CM factor partially contributes to the DEP force. Furthermore, for small particles the surface conductance effect in the electric double layer influences the particles conductivity and hence the DEP response [31]. The width of the electric double layer is altered with changing ion concentration in the solution which again influences the CM factor. Therefore, when relating measured particle velocities to the device performance it should be verified that the DEP response of the particle was not altered by increasing conductivities. A large particle ($\geqslant$10 μm) has a relative constant CM factor (only ~10% change on CM) for increasing conductivities while smaller particles (~1 μm) can undergo significant changes (figure 4(c)). Also, the CM factor considers ideal dielectric spherical particles and medium. More complex particles (e.g. cells, protein, DNA) and below size scales of 10^{-6} μm the application of the CM factor has limitations [32]. Moreover, at higher conductivities (>50 mS m^{-1}) electrothermal effects from temperature gradients due to

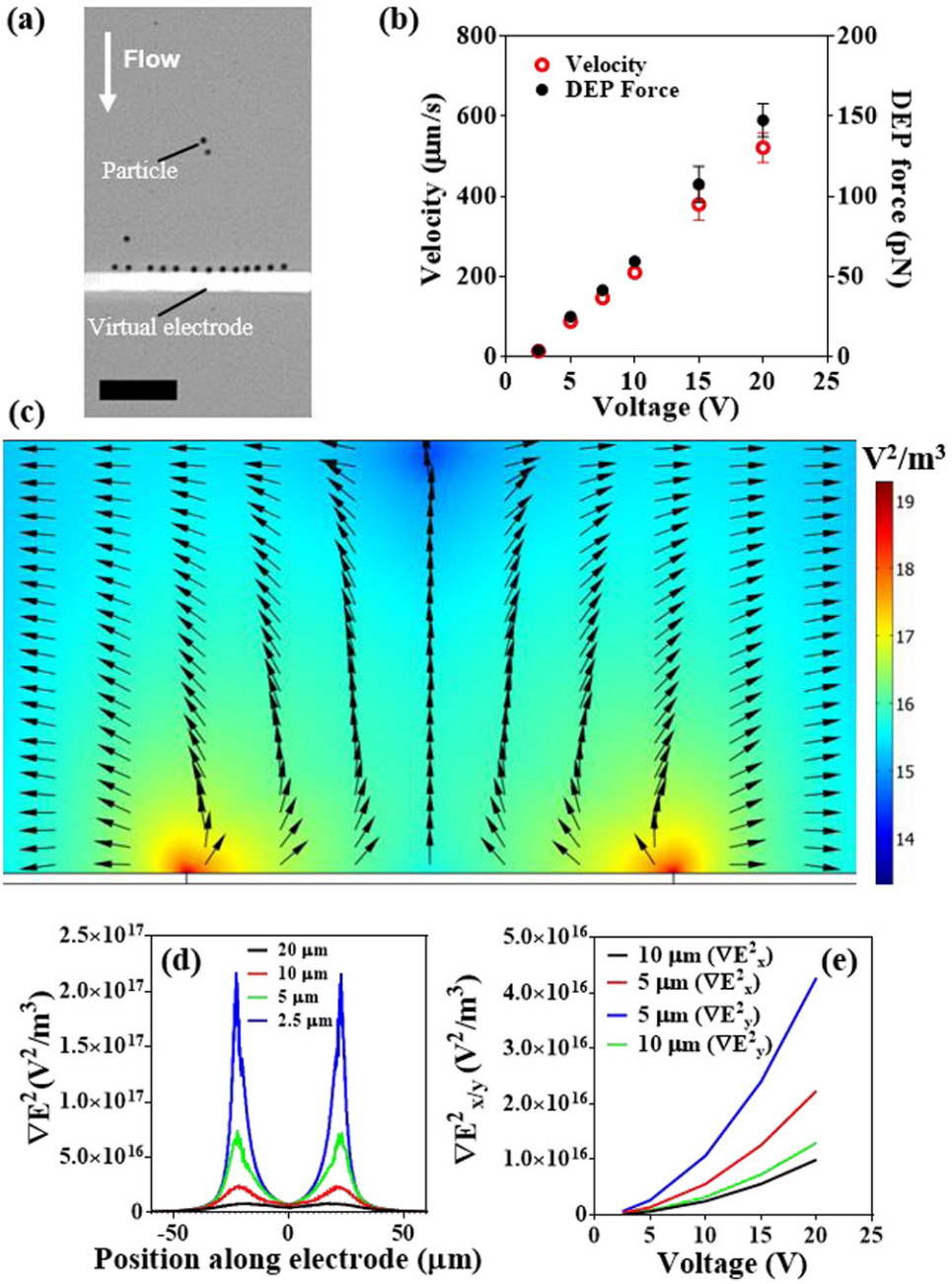

Figure 3. (a) Principle of estimation of DEP force through retention of particles. Drag force was balanced against the negative DEP force (Scale bar: 100 μm). (b) Velocity and corresponding DEP force experienced by 10 μm particles for varying voltages at 50 kHz, 5 mS m^{-1}, a light intensity of 2 W cm^{-2}, a channel height of 40 μm and an electrode width of 40 μm. (c) Simulation of electric field in the OET device of 40 μm height and a 45 μm virtual electrode pattern at 50 kHz and 20 V in a 5 mS m^{-1} conductivity solution. The gradient of the electric field squared ($\log_{10}\nabla E^2$) is shown as surface plot where the colour bar represents the magnitude. The black arrows show the direction of the DEP force for particles experiencing negative DEP. (d) Electric field distribution at different distances above the photoconductor and along the 45 μm virtual electrode pattern. (e) The field components ∇E_y^2 and ∇E_x^2 at the edge of the virtual electrode were simulated for different voltages and different distance to the photoconductor surface.

Joule heating can drive microflows which can compete with electrokinetic effects like DEP [33]. Temperature increases by illumination of the photoconductor can be excluded in the OET chip due to low optical intensities (2 W cm^{-2}) [34]. The high electric fields (10^5 V m^{-1}) generated in the OET chip suggest the ability to produce Joule heating and promote electrothermal microflows. However, at higher conductivities the applied voltage drops mainly across the photoconductor producing low field strength in the liquid which combined with the low channel height [35] suppresses electrothermal microflows.

The retention performance of the OET device for various conductivities was investigated (figure 4(d)). Velocities of 522 μm s^{-1} to 17 μm s^{-1} were measured for conductivities of 5 mS m^{-1} to 100 mS m^{-1}. This corresponded to DEP forces of 150 pN to 5 pN. A sharp drop in the DEP force occurred within

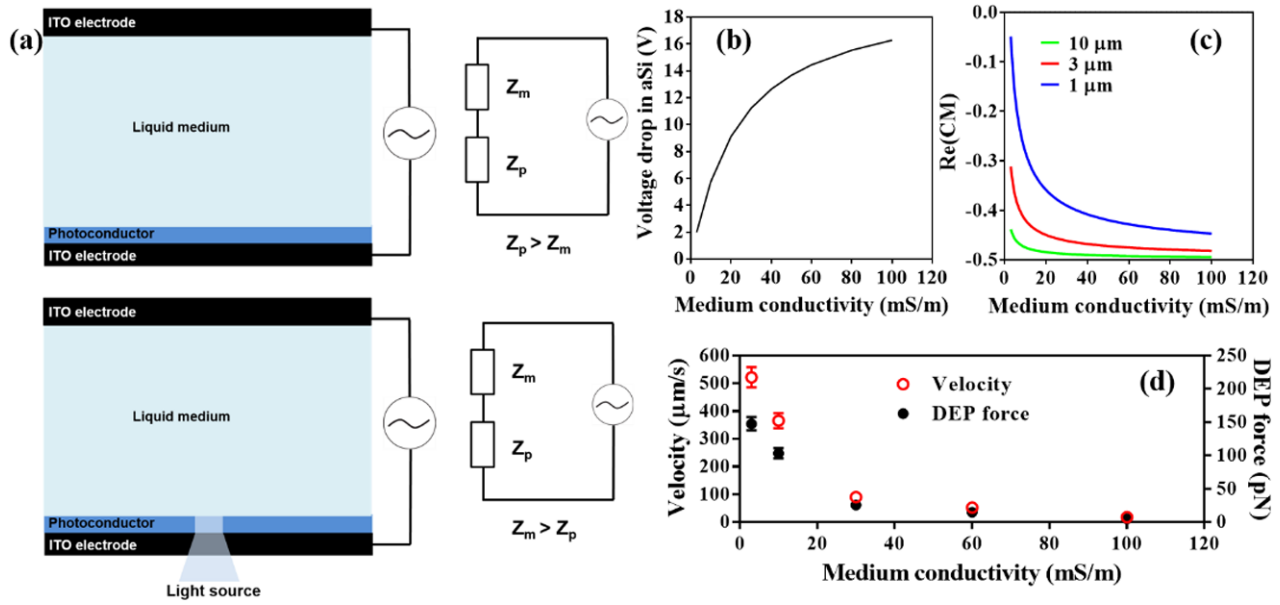

Figure 4. (a) Schematic of OET device with and without illumination and the corresponding equivalent circuit. (b) Modelled voltage drop across the photoconductor for different conductivities. (c) The change of the CM factor for different particles sizes when the medium conductivity increases. (d) Experimental results showing decreasing velocities and DEP forces experienced by 10 um particles for increasing medium conductivities (50 kHz, 20 V, 2 W cm^{-2}).

the range from 5 mS m^{-1} to 30 mS m^{-1} before it levelled off slightly towards higher conductivities up to 100 mS m^{-1}. This compared well with simulations of the voltage drop across the aSi layer, where more than half of the applied voltage dropped across the layer within 30 mS m^{-1} to 40 mS m^{-1} before a levelling could be observed. The results gave insight in the operation limits of the OET device. This is of importance especially when dealing with mammalian cells suspended in buffer solutions where certain parameters such as pH, ion concentrations or osmolarity are adjusted to maintain a viable cell population. A cell sample is usually suspended in specialised cell media or buffer solutions with high conductivities of $\geqslant$1 S m^{-1}. These media are not applicable for a conventional OET device. The electric field in the liquid layer would become 3 to 4 magnitudes lower ($\nabla E^2 \sim 10^{13}$–10^{14} V^2 m^{-3}) resulting in DEP forces not sufficient for continuous particle manipulation. However, a Ph-OET device developed by Hsu *et al* was capable of overcoming this restriction and enabled cell and particle handling in cell culture medium [36].

3.2.3. Influence of gap between the electrodes (channel height). The performance of the OET chip can be improved by considering how the electric field is dependent on the gap between photoconductor and the ITO electrode. The voltage drop across the liquid layer reduces while the electric field magnitude increases when decreasing the gap between the photoconductor and the ITO electrode. Simulations of the electric field gradient ∇E^2 were carried out to obtain insight into the significance of channel heights in the OET device. In figures 5(a) and (b), ∇E^2 is shown for varying electrode gaps. In particular, figure 5(a) shows the decay of ∇E^2 above the edge of a virtual electrode for electrode gaps of 15 μm to 110 μm. The field distribution is shown for the first 15 μm above the illuminated aSi layer. The increase in the channel height decreases the field magnitude and promotes a steeper decay above the photoconductor. Furthermore, larger particles experience a greater volume of the channel and so we need to consider how the field varies higher up in the channel where the change in the magnitude becomes more pronounced (figure 5(b)). Therefore, the OET device performance is significantly influenced by the device dimensions combined with the particle size. The device fabrication method introduced above enables the construction of variable and well controlled SU8 thickness. With that the performance change was tested by creating channels with heights of 70 μm and 15 μm. A 20 μm virtual electrode (2 W cm^{-2}) and an AC signal of various voltages at 100 kHz were used for retention experiments of 6 μm particles suspended in a medium of 5 mS m^{-1} (figure 5(c)). Using a channel height of 15 μm the obtained DEP forces for voltages of 6.5 V–20 V were 16 pN to 132 pN while at a gap of 70 μm the obtained DEP forces were only 3 pN to 22 pN. As the channel's height was reduced the impedance of the liquid layer decreased, decreasing the voltage dropped across it so that the field did not increase linearly with decreased channel height. Our results show that despite this, the forces obtainable increase at a greater rate than the channel height decreases which can be understood by considering that making the channel smaller has the same geometrical effects as considering larger particles [37].

These results demonstrated that relatively fast manipulation of small particles is feasible but requires good dimensional control over the conventional OET device structure. However, reducing the electrode gap is also accompanied with an increased shear stress imposed onto particles. While this is less important for artificial particles, mammalian cells might be affected, although some cells (e.g. red blood cells) are able to withstand higher shear rates. Furthermore, high sample concentration (10^7–10^8 beads ml^{-1} with particle diameters >5 μm)

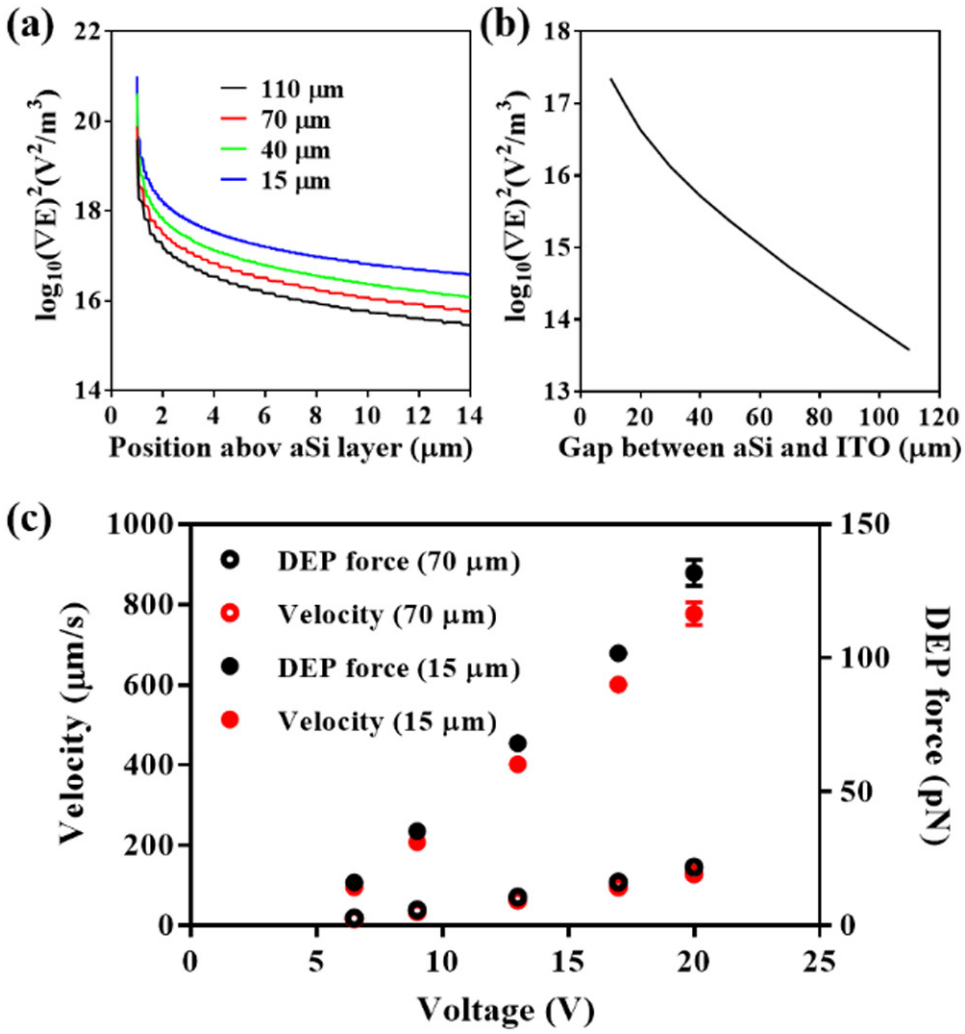

Figure 5. (a) Simulated magnitude of the electric field gradient for a range of gap heights (15–110 μm) and a virtual electrode width of 20 μm, an AC signal of 20 V at 100 kHz and a liquid medium conductivity of 5 mS m^{-1}, 15 μm above the edge of the virtual electrode. (b) Simulation of electric field gradient in the centre of the microchannel cross section and above the edge of a 20 μm virtual electrode for various gaps. (c) Retention experiments of 6 μm particles under continuous flow using a 20 μm virtual electrode at 100 kHz, in medium with 5 mS m^{-1} conductivity and a light intensity of 2 W cm^{-2}. Velocity of particles and corresponding DEP force against voltages applied to OET devices of different channel heights.

should be avoided as channel blocking by particle aggregates inhibits efficient manipulations.

3.2.4. Light pattern size and intensity. The device performance was dependent on several factors as shown above and each of these need to be adjusted to obtain forces of appropriate magnitude for particle manipulation under continuous flow. Moreover, the virtual electrode projected on to the photoconductor is an additional independent parameter that requires adjustment. The magnitude of the light intensity which is projected onto the photoconductor through an objective influences the magnitude of the electric field in the sample. The light intensity increases with increasing magnification and hence increases the conductivity of the aSi layer. Also, the dimension of the electrode (e.g. width) as well as the pixel intensity of the virtual electrode defined by the imaging software influence the electric field created in the liquid medium. We show that the virtual electrode width and transparency (pixel intensity) can be used to tune the electric field magnitude and hence the DEP force experienced by the particle. Experiments were carried out with increasing virtual electrode width (7 μm to 120 μm) and increasing electrode transparency (0% to 60%). Again, retention of 6 μm particles under continuous flow were investigated using an OET chip with 15 μm gap height, a voltage signal of 10 V and 15 V at 100 kHz in a medium of 5 mS m^{-1}. The virtual electrode width was varied between 7 μm and 120 μm (figure 6(a)). The measured velocities for that width range were between 54 μm s^{-1} and 300 μm s^{-1} (figure 6(b)) which corresponded to DEP forces of 9 pN to 51 pN.

A non-linear behaviour characterised by rapid increase in the DEP force was observed when increasing the virtual electrode width from 7 μm to 20 μm followed by saturation of the force for width of more than 20 μm. This device behaviour may be associated with the change of the gradient of the electric field across the channel height at constant voltage. Simulation of the electric field gradient for several electrode widths showed similar magnitudes of the field close the

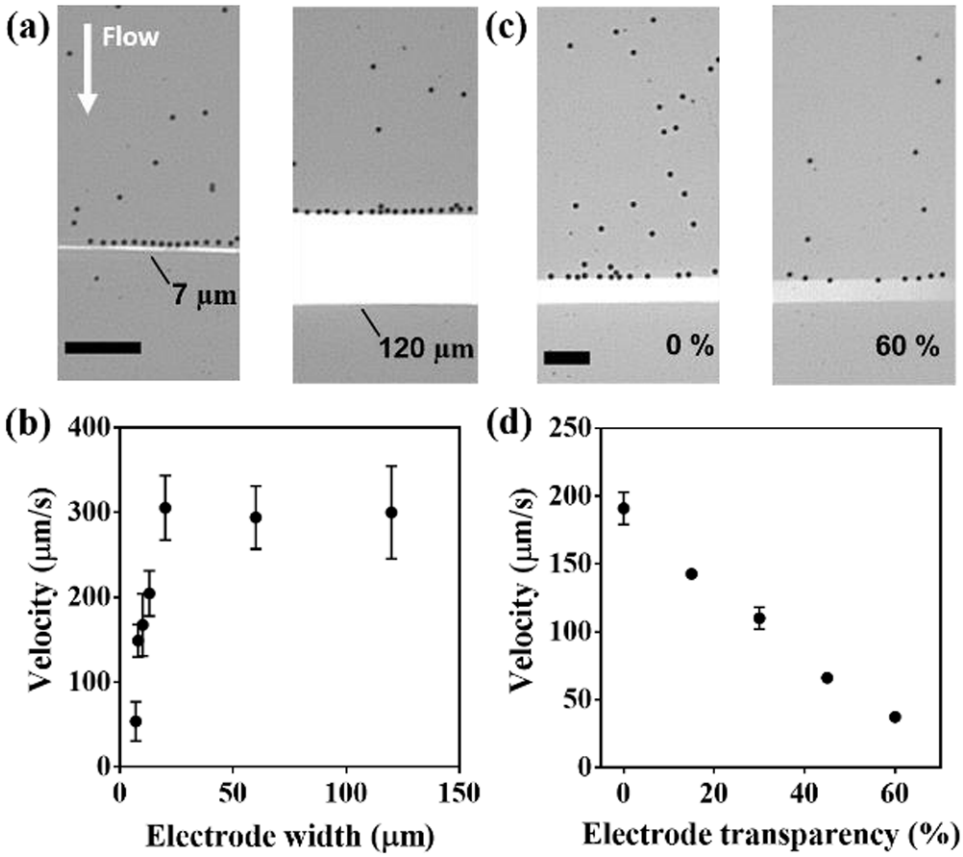

Figure 6. (a) Images of the retention experiment of 6 μm particles using different electrode widths (Scale bar: 100 μm). (b) Influence of the width of the virtual electrode pattern on particle retention under continuous flow (100 kHz, 15 V, 5 mS m^{-1}, 2 W cm^{-2}). (c) Images from the experiment showing the virtual electrodes unaltered (0%) and with increased (60%) transparency (Scale bar: 50 μm). (d) Influence of the transparency (set by imaging software) of the virtual electrode pattern (30 μm) on particle retention at 100 kHz (10 V, 5 mS m^{-1}, 12 W cm^{-2}).

photoconductor surface (<5 μm) (figure S5). However, the field strength above the surface decayed much steeper for the 7 μm electrode. An increasing electrode width resulted in a convergence of ∇E^2 which agreed well with the asymptotic behaviour observed in the experiments. In addition, reflection at the interfaces in the OET device may alter the light intensity which reaches the photoconductor. This influence may be pronounced when using small virtual electrode patterns and could affect the photoconductivity of the aSi layer.

The light intensity of a virtual electrode can be easily changed by defining the pixel intensity in the imaging software. This gives spatial fine control over the DEP force. Altering the pixel intensity or transparency from 0% to 60% (0% being full intensity of 2 W cm^{-2} and 60% being reduced intensity, figure 6(c)) resulted in retention velocities of 190 μm s^{-1} to 37 μm s^{-1} with corresponding DEP forces of 11 pN to 2 pN (figure 6(d)). Thus, controlling the light pattern enables the generation of tuneable electric field gradients with corresponding DEP forces at arbitrary positions in the OET device, while other parameters (e.g. voltage, frequency, objective) can be kept constant. For instance, this can be used to selectively manipulate particles of different sizes.

3.3. Continuous particle manipulation

Conventional dielectrophoresis with fixed metal electrodes has been commonly applied for different microfluidic operations under pressure driven flows. Examples included focussing of particles into a single stream [38, 39] or separation of a particle mixture [40] based on physical properties (e.g. volume). Focussing particles into tight streams can be considered as an essential step in microfluidic flow cytometer [41, 42] where the properties (e.g. fluorescence) of single particles can be investigated prior to subsequent processes (e.g. separation, detection). It can also be used to concentrate particles into specific regions within the microchannel for counting, detecting, enrichment purposes [43] or to separate particles from a carrier liquid [44–46] (e.g. washing, functionalisation). Here we demonstrate that that the developed OET device can create arbitrary virtual electrode patterns in real time and that these can be used for particle concentration, focussing and sorting. Figure 7(a) shows the focussing of particles into the centre of the channel. In this case the DEP and Stokes drag force experienced by the particles combined to a net force that guided particles along the virtual electrode. This resulted in particles being lined up once past the electrode pattern.

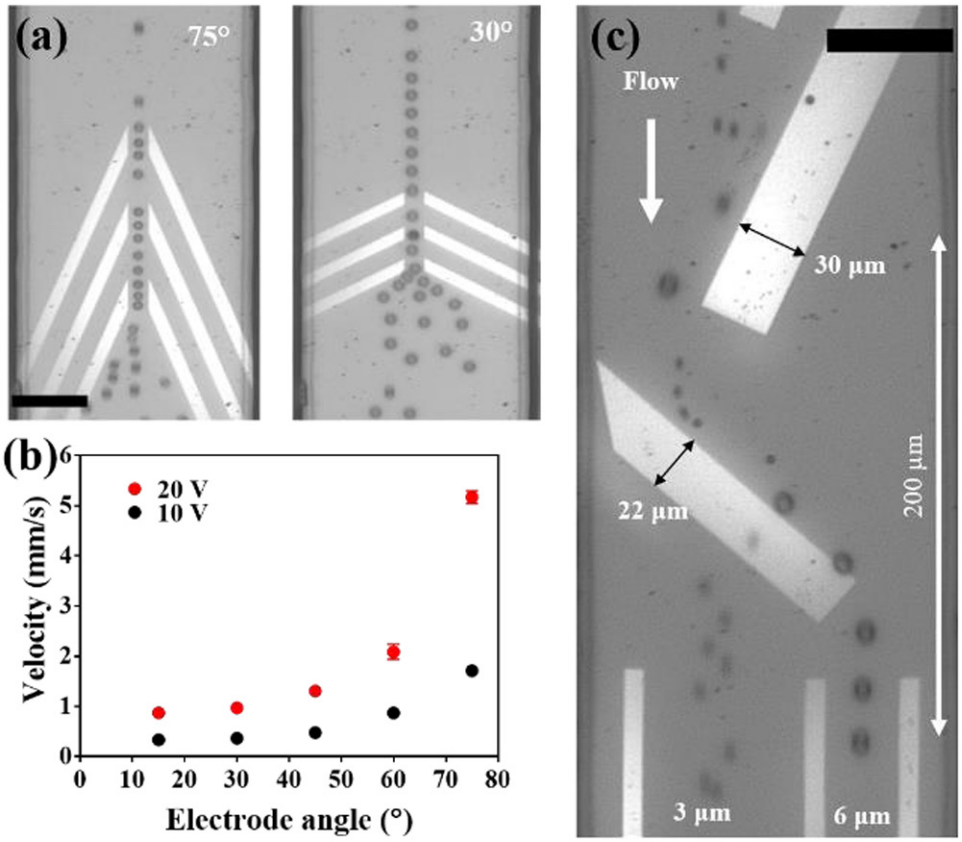

Figure 7. (a) Examples of focusing experiments of 6 μm particles under continuous flow using angled virtual electrodes (Scale bar: 50 μm). (b) Velocity of focused 6 μm particles depending on electrode angle and voltage signal using 10 μm wide electrodes (2 W cm^{-2}) at 100 kHz in 5 mS m^{-1} medium and a 15 μm height OET chip. (c) Guiding and separation of 6 μm and 3 μm beads into virtual microchannels at 100 kHz, 15 V (Movie S1). An oblique virtual electrode of 22 μm width imposed a larger DEP force on 6 μm particles which were deflected along the electrode while 3 μm particles passed the virtual electrode with minor deflection (Scale bar: 50 μm).

Combined with the hydrodynamic force under laminar flow conditions a stable and tight single stream of particles was maintained. Depending of the angle (15°–75°) of the virtual electrodes and the applied voltage signal (10 V, 20 V) particles with velocities of 0.4 mm s^{-1} to 5 mm s^{-1} were tightly focussed into single particle stream (figure 7(b)). Compared to previous studies on OET devices, these results demonstrated improved particle manipulation speed with velocities in the mm/s range using oblique virtual electrodes combined with a shallow microchannel geometry. This will be of use for application such as a microfluidic flow cytometer where flexible electrode arrangements suited for different kinds of particles would give the device a greater flexibility through real time reconfiguration although it would not be able to compete on speed with state of the art flow cytometers using velocities of 1 m s^{-1} to 10 m s^{-1} for high throughput analysis (500 000 particles s^{-1}) [47].

Channel integrated OET devices can also be utilized for particle sorting, which may reduce the complexity of a cytometer setup. A simple example is shown in figure 7(c) where a particle mixture was guided towards a separation zone consisting of an angled virtual electrode with width of 22 μm and two virtual channels (Movie S1). While flow rate and voltage signal were kept constant, the electrode width was adjusted to achieve a separation between the particle sizes. While the negative DEP force was sufficient for deflecting 6 μm particles, the drag force on 3 μm particles dominated causing these particles to pass the virtual electrode with only minor deflection. Furthermore, oblique electrodes can also be used to deflect particles laterally in a microfluidic channel (figure S6). The channel integration then has a second advantage in that different patterns with multiple inlets or outlets can be integrated into the design in the same layer that defines the channel height. This could be used for automated biological assays integrated into continuous microfluidic assays. Such a concept has been shown using solid rails which guide particle across several adjacent laminar streams [46]. Each stream can carry a certain reagent to wash and modify (e.g. protein coupling, surface functionalisation) particles prior to a reaction in another laminar stream which carries a sample liquid (e.g. blood) with an analyte of interest. The size based response of the DEP force may also be used for the separation of cell populations (e.g. white bloods cell from red blood cell or malaria infected cells) or in droplet microfluidics to maintain monodispersity.

3.4. Limitations

The device characterisation experiments showed unwanted particle–particle and particle–wall interactions. This was

attributed to a voltage drop into the liquid medium in the absence of illuminations of the photoconductor but when applying a voltage signal. It resulted in a leaked and mainly uniform electric field within the channel that interacted with suspended particles and causing a weak non-uniform field distribution along the channel walls. The former caused particle–particle interactions due to mutual dielectrophoresis. This pearl-chaining effect is the result of the uniform field being spatially altered creating low and high field regions around the particle surface. The latter was caused by the insulating properties of SU8. The electric field strength being low close to the SU8 wall forced particles to move towards the channel boundaries occasionally.

The leakage fields can be explained by the fact that the used photoconductor was not an ideal insulator in the absence of illumination. Then a combination of voltage amplitudes and low medium conductivities created these leakage fields. To address this problem without increasing medium conductivities and sacrificing strong DEP forces the thickness of the photoconductor can be increased. While this seems trivial because deposition of thicker photoconductor films can be easily performed, our trials with increased film thickness showed residual stresses in these films leading to delamination or blistering. The deposition process has to be optimised to create stable films. Moreover, an increase in the thickness of the photoconductor may require increased optical power because of a relative high absorption coefficient within 1 μm of aSi which otherwise would not fully increase the photoconductivity throughout the layer.

4. Conclusion

A method for integrating a conventional OET arrangement into a microfluidic chip was introduced in this work. We have demonstrated the importance of channel geometry in the OET device and developed a method to finely control the channel dimensions. To achieve this negative photoresist SU8 3000 series was used and a novel step of attaching the top slide before photopatterning the resist was produced. The advantages of this method were low bonding temperature (65 °C to 95 °C), homogenous bonding area, stability to organic solvents for cleaning purposes and flexibility in creating microchannels of various heights and patterns. The device characterisation showed that the device performance can be tuned by controlling a range of parameters including the voltage signal, channel heights, the virtual electrode size and transparency. The flexibility of quickly creating virtual electrodes of arbitrary shape and intensity allows useful microfluidic functions including particle focussing which can be combined with continuous subsequent particle separation steps.

Acknowledgments

The authors wish to acknolwege the support of an RAEng/EPSRC fellowship which supported a period of this work EP/G058393/1. We thank the James Watt Nanofabrication Centre (Glasgow, UK) for help with device fabrication.

ORCID iDs

Christian Witte https://orcid.org/0000-0003-3023-7968
Julien Reboud https://orcid.org/0000-0002-6879-8405
Jonathan M Cooper https://orcid.org/0000-0002-2358-1050
Steven L Neale https://orcid.org/0000-0002-4588-276X

References

[1] Chiou P Y, Ohta A T and Wu M C 2005 Massively parallel manipulation of single cells and microparticles using optical images *Nature* **436** 370–2
[2] Berkely Lights Inc. (https://www.berkeleylights.com/)
[3] Lee S, Park H J, Yoon J S and Kang K H 2010 Optoelectrofluidic field separation based on light-intensity gradients *Biomicrofluidics* **4** 034102
[4] Ohta A T, Chiou P Y, Han T H, Liao J C, Bhardwaj U, McCabe E R B, Yu F Q, Sun R and Wu M C 2007 Dynamic cell and microparticle control via optoelectronic tweezers *J. Microelectromech. Syst.* **16** 491–9
[5] Ohta A T, Chiou P Y, Phan H L, Sherwood S W, Yang J M, Lau A N K, Hsu H Y, Jamshidi A and Wu M C 2007 Optically controlled cell discrimination and trapping using optoelectronic tweezers *IEEE J. Sel. Top. Quantum* **13** 235–43
[6] Hoeb M, Radler J O, Klein S, Stutzmann M and Brandt M S 2007 Light-induced dielectrophoretic manipulation of DNA *Biophys. J.* **93** 1032–8
[7] Chiu T K, Chou W P, Huang S B, Wang H M, Lin Y C, Hsieh C H and Wu M H 2016 Application of optically-induced-dielectrophoresis in microfluidic system for purification of circulating tumour cells for gene expression analysis-Cancer cell line model *Sci. Rep.* **6** 32851
[8] Valley J K, Ohta A T, Hsu H Y, Neale S L, Jamshidi A and Wu M C 2009 Optoelectronic tweezers as a tool for parallel single-cell manipulation and stimulation *IEEE Trans. Biomed. Circuits Syst.* **3** 424–31
[9] Lee Y H, Wang C H and Lee G B 2013 Different optical images for optically-induced electroporation of multiple gene transfection *Proc. IEEE Micro Electro* pp 907–10
[10] Kremer C, Witte C, Neale S L, Reboud J, Barrett M P and Cooper J M 2014 Shape-dependent optoelectronic cell lysis *Angew. Chem., Int. Ed. Engl.* **53** 842–6
[11] Lin Y H and Lee G B 2009 An optically induced cell lysis device using dielectrophoresis *Appl. Phys. Lett.* **94** 033901
[12] Witte C, Kremer C, Chanasakulniyom M, Reboud J, Wilson R, Cooper J M and Neale S L 2014 Spatially selecting a single cell for lysis using light-induced electric fields *Small* **10** 3026–31
[13] Liang W F, Zhao Y L, Liu L Q, Wang Y C, Li W J and Lee G B 2017 Determination of cell membrane capacitance and conductance via optically induced electrokinetics *Biophys. J.* **113** 1531–9
[14] Valley J K, Swinton P, Boscardin W J, Lue T F, Rinaudo P F, Wu M C and Garcia M M 2010 Preimplantation mouse embryo selection guided by light-induced dielectrophoresis *PLoS One* **5** e10160
[15] Ohta A T, Garcia M, Valley J K, Banie L, Hsu H Y, Jamshidi A, Neale S L, Lue T and Wu M C 2010 Motile and non-motile sperm diagnostic manipulation using optoelectronic tweezers *Lab Chip* **10** 3213–7
[16] Hwang H, Lee D H, Choi W J and Park J K 2009 Enhanced discrimination of normal oocytes using optically induced pulling-up dielectrophoretic force *Biomicrofluidics* **3** 14103
[17] Jamshidi A, Neale S L, Yu K, Pauzauskie P J, Schuck P J, Valley J K, Hsu H Y, Ohta A T and Wu M C 2009 NanoPen: dynamic, low-power, and light-actuated patterning of nanoparticles *Nano Lett.* **9** 2921–5

[18] Zhang S L, Juvert J, Cooper J M and Neale S L 2016 Manipulating and assembling metallic beads with Optoelectronic Tweezers *Sci. Rep.* **6** 32840
[19] Chow E M *et al* 2017 Micro-object assembly with an optically addressed array *2017 19th Int. Conf. on Solid-State Sensors, Actuators and Microsystems (Transducers)* pp 682–5
[20] Tien M C, Ohta A T, Yu K, Neale S L and Wu M C 2009 Heterogeneous integration of InGaAsP microdisk laser on a silicon platform using optofluidic assembly *Appl. Phys.* A **95** 967–72
[21] Juvert J, Zhang S L, Eddie I, Mitchell C J, Reed G T, Wilkinson J S, Kelly A and Neale S L 2016 Micromanipulation of InP lasers with optoelectronic tweezers for integration on a photonic platform *Opt. Express* **24** 18163–75
[22] Zhang S L *et al* 2019 The optoelectronic microrobot: A versatile toolbox for micromanipulation *Proc. Natl Acad. Sci. USA* **116** 14823–8
[23] Lin Y H and Lee G B 2010 An integrated cell counting and continuous cell lysis device using an optically induced electric field *Sensors Actuators* B **145** 854–60
[24] Yang S-M, Yu T-M, Liu M-H, Hsu L and Liu C-H 2011 Moldless PEGDA-based optoelectrofluidic platform for microparticle selection *Adv. Optoelectron.* **2011** 1–8
[25] Chou W P, Wang H M, Chang J H, Chiu T K, Hsieh C H, Liao C J and Wu M H 2017 The utilization of optically-induced-dielectrophoresis (ODEP)-based virtual cell filters in a microfluidic system for continuous isolation and purification of circulating tumour cells (CTCs) based on their size characteristics *Sensors Actuators* B **241** 245–54
[26] Liang W F, Zhao Y L, Liu L Q, Wang Y C, Dong Z L, Li W J, Lee G B, Xiao X B and Zhang W J 2014 Rapid and label-free separation of Burkitt's lymphoma cells from red blood cells by optically-induced electrokinetics *PLoS One* **9** e90827
[27] Huang K W, Wu Y C, Lee J A and Chiou P Y 2013 Microfluidic integrated optoelectronic tweezers for single-cell preparation and analysis *Lab Chip* **13** 3721–7
[28] Pethig R 2010 Dielectrophoresis: status of the theory, technology, and applications *Biomicrofluidics* **4** 022811
[29] Svoboda K and Block S M 1994 Biological applications of optical forces *Annu. Rev. Biophys.* **23** 247–85
[30] Zhang S *et al* 2018 Escape from an optoelectronic tweezer trap: experimental results and simulations *Opt. Express* **26** 5300–9
[31] Hughes M P, Morgan H and Flynn M F 1999 The dielectrophoretic behavior of submicron latex spheres: influence of surface conductance *J. Colloid Interface Sci.* **220** 454–7
[32] Pethig R 2019 Limitations of the Clausius–Mossotti function used in dielectrophoresis and electrical impedance studies of biomacromolecules *Electrophoresis* **40** 2575–83
[33] Salari A, Navi M, Lijnse T and Dalton C 2019 AC electrothermal effect in microfluidics: a review *Micromachines* **10** 762
[34] Valley J K, Jamshidi A, Ohta A T, Hsu H Y and Wu M C 2008 Operational regimes and physics present in optoelectronic tweezers *J. Microelectromech. Syst.* **17** 342–50
[35] Salari A, Navi M and Dalton C 2015 A novel alternating current multiple array electrothermal micropump for lab-on-a-chip applications *Biomicrofluidics* **9** 014113
[36] Hsu H Y, Ohta A T, Chiou P Y, Jamshidi A, Neale S L and Wu M C 2010 Phototransistor-based optoelectronic tweezers for dynamic cell manipulation in cell culture media *Lab Chip* **10** 165–72
[37] Zhang S, Li W, Elsayed M, Tian P, Clark A W, Wheeler A R and Neale S L 2019 Size-scaling effects for microparticles and cells manipulated by optoelectronic tweezers *Opt. Lett.* **44** 4171–4
[38] Lin C H, Lee G B, Fu L M and Hwey B H 2004 Vertical focusing device utilizing dielectrophoretic force and its application on microflow cytometer *J. Microelectromech. Syst.* **13** 923–32
[39] Holmes D, Morgan H and Green N G 2006 High throughput particle analysis: combining dielectrophoretic particle focussing with confocal optical detection *Biosens. Bioelectron.* **21** 1621–30
[40] Khoshmanesh K, Zhang C, Tovar-Lopez F J, Nahavandi S, Baratchi S, Kalantar-Zadeh K and Mitchell A 2009 Dielectrophoretic manipulation and separation of microparticles using curved microelectrodes *Electrophoresis* **30** 3707–17
[41] Huh D, Gu W, Kamotani Y, Grotberg J B and Takayama S 2005 Microfluidics for flow cytometric analysis of cells and particles *Physiol. Meas.* **26** R73–98
[42] Godin J, Chen C H, Cho S H, Qiao W, Tsai F and Lo Y H 2008 Microfluidics and photonics for bio-system-on-a-chip: a review of advancements in technology towards a microfluidic flow cytometry chip *J. Biophotonics* **1** 355–76
[43] Xuan X C, Zhu J J and Church C 2010 Particle focusing in microfluidic devices *Microfluid. Nanofluid.* **9** 1–16
[44] Hu X Y, Bessette P H, Qian J R, Meinhart C D, Daugherty P S and Soh H T 2005 Marker-specific sorting of rare cells using dielectrophoresis *Proc. Natl Acad. Sci. USA* **102** 15757–61
[45] Kim U, Qian J R, Kenrick S A, Daugherty P S and Soh H T 2008 Multitarget dielectrophoresis activated cell sorter *Anal. Chem.* **80** 8656–61
[46] Sochol R D, Li S, Lee L P and Lin L W 2012 Continuous flow multi-stage microfluidic reactors via hydrodynamic microparticle railing *Lab Chip* **12** 4168–77
[47] Piyasena M E and Graves S W 2014 The intersection of flow cytometry with microfluidics and microfabrication *Lab Chip* **14** 1044–59